



**HAL**  
open science

## Structural-Stability Study of Antiperovskite Na<sub>3</sub>OCl for Na-Rich Solid Electrolyte

Tan-Lien Pham, Woon Ih Choi, Aamir Shafique, Hye Jung Kim, Munbo Shim, Kyoungmin Min, Won-Joon Son, Inkook Jang, Dae Sin Kim, Mauro Boero, et al.

► **To cite this version:**

Tan-Lien Pham, Woon Ih Choi, Aamir Shafique, Hye Jung Kim, Munbo Shim, et al.. Structural-Stability Study of Antiperovskite Na<sub>3</sub>OCl for Na-Rich Solid Electrolyte. *Physical Review Applied*, 2023, 19 (3), pp.034004. 10.1103/PhysRevApplied.19.034004 . hal-04281598

**HAL Id: hal-04281598**

**<https://hal.science/hal-04281598>**

Submitted on 14 Nov 2023

**HAL** is a multi-disciplinary open access archive for the deposit and dissemination of scientific research documents, whether they are published or not. The documents may come from teaching and research institutions in France or abroad, or from public or private research centers.

L'archive ouverte pluridisciplinaire **HAL**, est destinée au dépôt et à la diffusion de documents scientifiques de niveau recherche, publiés ou non, émanant des établissements d'enseignement et de recherche français ou étrangers, des laboratoires publics ou privés.

# Structural stability study of antiperovskite $\text{Na}_3\text{OCl}$ for Na-rich solid electrolyte

Tan-Lien Pham,<sup>1, a)</sup> Woon Ih Choi,<sup>2, b)</sup> Aamir Shafique,<sup>1</sup> Hye Jung Kim,<sup>3</sup> Munbo Shim,<sup>2</sup> Kyoungmin Min,<sup>4</sup> Won-Joon Son,<sup>2</sup> Inkook Jang,<sup>2</sup> Dae Sin Kim,<sup>2</sup> Mauro Boero,<sup>5</sup> Carlo Massobrio,<sup>5</sup> Guido Ori,<sup>5</sup> Hyo Sug Lee,<sup>6</sup> and Young-Han Shin<sup>1, c)</sup>

<sup>1)</sup> *Multiscale Materials Modeling Laboratory, Department of Physics, University of Ulsan, Ulsan 44610, Republic of Korea*

<sup>2)</sup> *Computational Science and Engineering (CSE) Team, Innovation Center, Samsung Electronics, Hwaseong-si 18448, Republic of Korea*

<sup>3)</sup> *Department of Physics, Pusan National University, Busan 46241, Republic of Korea*

<sup>4)</sup> *School of Mechanical Engineering, Soongsil University, 369 Sangdo-ro, Dongjak-gu, Seoul 06978, Republic of Korea*

<sup>5)</sup> *Université de Strasbourg, CNRS, Institut de Physique et Chimie des Matériaux de Strasbourg, UMR 7504, F-67034 Strasbourg, France*

<sup>6)</sup> *Samsung Advanced Institute of Technology, Suwon 16678, Republic of Korea*

The structural phase transition of the high symmetry cubic phase of antiperovskite  $\text{Na}_3\text{OCl}$  is investigated by computing the phonon band structures of 14 different polymorphs with distinct types of  $\text{ONa}_6$  octahedral tilting. The resulting  $P$ - $T$  phase diagram shows that, at high temperature and low pressure, the high-symmetry cubic structure with  $\text{Pm}\bar{3}\text{m}$  symmetry is the most stable phase. At low temperature and high pressure, on the other hand, the monoclinic structure with  $\text{P2}_1/\text{m}$  symmetry becomes the most stable phase. In between those two, there is a region in the phase diagram where the orthorhombic structure with  $\text{Bmmb}$  symmetry is the most stable phase. To improve upon the quasi-harmonic results, we did additional calculations in the framework of the self-consistent phonon (SCP) theory, including lattice anharmonicity by using cubic and quartic interatomic force constants (IFCs). This is particularly important for the high-symmetric cubic phase. We find that by decreasing the temperature, the frequency of soft phonon at the  $M$  and  $R$  symmetry points shift gradually to lower values. From these results we can infer that a phase transition occurs around 166 - 195 K upon soft-mode condensation. Due to the proximity of the soft mode frequencies at both symmetry points  $R$  and  $M$ , we expect a cubic-to-orthorhombic phase transition to be realized via simultaneous condensation of the two octahedral tilting modes.

## I. INTRODUCTION

While Li-ion batteries have been widely used in portable electronic devices and electric vehicles due to their high performance, their prospects in large-scale grid-level storage of renewables are severely restricted by the limited availability of Li.<sup>1-3</sup> Because of the higher abundance of Na compared to Li,<sup>4,5</sup> Na-ion batteries have been recently gaining attention.<sup>6,7</sup> In addition, to minimize the hazards such as leakage of corrosive, toxic, and flammable organic liquid electrolytes, solid electrolytes have been suggested as alternatives to conventional liquid electrolytes,<sup>8-10</sup> and the studies of solid electrolytes such as alkali metal oxyhalides attract much attention.<sup>1,7,11-13</sup>

In our previous work, we performed first-principles calculations for 14 different octahedrally tilted  $\text{Na}_3\text{OCl}$  structures, and found that they are energetically more stable than the high symmetric cubic phase by 11 - 16 meV per stoichiometric unit. Phonon spectra, computed within the harmonic approximation, have shown that

the monoclinic phase with  $\text{P2}_1/\text{m}$  symmetry and the orthorhombic phase with symmetry  $\text{Pnma}$  have no imaginary modes, thus providing a fingerprint of the stability of these systems. Yet, the absence of imaginary frequencies is not always a criterion sufficient to assess the stability of a system. Depending on the environmental conditions, the presence of imaginary modes can still correspond to stable systems. For example, well-known perovskite oxides such as  $\text{SrTiO}_3$ ,  $\text{BaTiO}_3$ , and  $\text{PbTiO}_3$  do have imaginary frequencies in the harmonic phonon band structure of its cubic phases that are stabilized above certain temperatures.<sup>14-16</sup> Likewise, to better understand phase transition characteristics of  $\text{Na}_3\text{OCl}$  that have the same symmetry, we need to consider the Gibbs free energy of its possible structures with respect to environmental parameters such as pressure and temperature.<sup>17</sup>

Until recently, information on the enthalpies of formation for the  $\text{Na}_3\text{OCl}$  and its thermodynamics properties and phase change were not available. Despite the experimental synthesis and identification of the cubic  $\text{Pm}\bar{3}\text{m}$  phase by Hippler *et al.*,<sup>11</sup> dating back to more than 30 years, only recently thorough characterizations have been reported.<sup>17,18</sup> Moreover, recent theoretical studies on a similar class of materials such as halide perovskites imply *the necessity of including lattice anharmonicity*, particularly, for the reliable prediction of phase transition temperature that matches well with available experimen-

<sup>a)</sup>These two authors contributed equally.

<sup>b)</sup>These two authors contributed equally.; Corresponding author; Electronic mail: wooni.choi@samsung.com

<sup>c)</sup>Corresponding author; Electronic mail: hoponpop@ulsan.ac.kr

tal data. For example, Tadano and Saidi calculated the cubic-to-tetragonal phase transition temperature of  $\alpha$ -CsPbBr<sub>3</sub> (404 - 423 K) by obtaining a very small difference from the experimental measurement (403 K).<sup>19</sup> For this outcome, they included the loop diagram that consists of quartic interatomic force constants (IFCs), and the contribution of the bubble self-energy term that consists of cubic IFCs on top of the self-consistent solution (SC1). Moreover, Tadano and Tsuneyuki found that lattice anharmonicity plays an important role in describing the lattice thermal conductivity of type-I clathrate Ba<sub>8</sub>Ga<sub>16</sub>Ge<sub>30</sub>.<sup>20</sup>

In many perovskite materials, the high symmetry cubic phase is stable at a high temperature, and with decreasing temperature, structures with lower symmetry such as tetragonal, orthorhombic, and monoclinic phases become stable. Therefore, in the harmonic phonon band structures of cubic SrTiO<sub>3</sub>, PbTiO<sub>3</sub>, and BaTiO<sub>3</sub> imaginary frequencies are found.<sup>14-16</sup> Both halide and oxide perovskites are well-known materials and an increasing amount of research reports their intriguing characteristics. Antiperovskites are structurally similar to perovskites. However, atomic positions occupied by cations in perovskites are replaced with anions in antiperovskites and *vice versa*. In terms of applications, antiperovskite alkali metal oxyhalides are good candidates for solid-state electrolytes.<sup>21</sup> Cubic Na<sub>3</sub>OCl has imaginary frequencies at the  $M$  and  $R$  modes, and 14 possible tilted systems are generated by combining  $M_3^+ \oplus R_4^+$  distortions that have lower static energy than the cubic phase.<sup>17</sup> In this paper, the stability of these 14 tilted phases, as well as the cubic phase, are discussed in terms of the Gibbs free energy using the quasi-harmonic approximation (QHA) method, which considers the effect of volume expansion to figure out the most stable phase and phase transition during the cooling down process.

To end this introduction, it is worth stressing that previous results for face-centered cubic metals such as silver and covalent materials such as diamond, graphite, and even the ionic materials such as lighter alkali hydrides (LiH, NaH) showed the effectiveness of phonon calculations for obtaining  $P$ - $T$  phase diagrams and thermodynamic properties using QHA.<sup>22-25</sup> Notwithstanding, another study on other metals such as Fe, Ni, Ti, and W showed that the thermodynamic quantities calculated with quasi-harmonic phonon calculations are particularly lacking in describing temperature dependence.<sup>26</sup> Moreover, many studies on the perovskite and antiperovskite materials show that careful consideration of lattice anharmonicity is essential for the reliable prediction of thermodynamic quantities as well as thermal conductivity and dielectric properties.<sup>14,27-30</sup>

This paper is organized in the following sections. Our methodologies are fully detailed in Sec. II, where we describe not only the harmonic and anharmonic approximations (treated within self-consistent phonon theory) but also the atomic-scale tools based on density functional theory. The results are presented in Sec. III. Some con-

clusions are collected in Sec. III C.

## II. METHODOLOGY OF CALCULATIONS

The harmonic approximation assumes that the second derivative of potential energy with respect to the atomic displacement is constant. This is a reasonably good approximation, particularly for the materials where the atoms are tightly bound through a strong covalent bond. In other words, the shape of the potential energy surface around the energy minimum is close to a parabolic shape for these materials. However, for the materials formed with the relatively weak bond between constituent atoms, the curvature around the energy minimum easily deviates from parabolic shape even with a displacement caused by the thermal excitation energy equivalent to room temperature. In this case, the anharmonic shape of the potential energy surface can be interpreted as the change of the effective harmonic frequency depending on the temperature.

For a certain class of materials, the harmonic approximation could be a cost-efficient and reliable way to model material properties. Moreover, there are well-established methods for calculating thermodynamics quantities out of phonon band structure calculations. However, for some materials that have strong lattice anharmonicity, higher-order force constants need to be considered for the reliable prediction of material properties. Herein, we first draw the  $P$ - $T$  phase diagram of Na<sub>3</sub>OCl through the Gibbs free energy calculated with the quasi-harmonic approximation (QHA). These calculations enable us to investigate phase change in a wide temperature and pressure range with a relatively small computational cost. Then, we move on to the anharmonic phonon calculations to examine the effect of lattice anharmonicity in the phase transition of the material. Since the number of interatomic force constants dramatically increases in case, the materials have low symmetry, so we selected the high-symmetry cubic phase only for this purpose.<sup>31,32</sup>

By expanding the harmonic phonon model of lattice dynamics, the QHA describes the thermal expansion of the material. In this approximation, phonon frequencies become volume-dependent while the harmonic approximation holds for each volume.<sup>33,34</sup> The QHA turns out to be a good approximation at temperatures far below the melting points<sup>35,36</sup> and many studies were performed with the QHA to predict the phase-dependent thermodynamic and elastic properties of the materials, which are consistent with experimental reports.<sup>15,22-24,37-43</sup>

The Gibbs free energy  $G(T, P)$  is an useful thermodynamic potential in the study of processes at constant temperature  $T$  and pressure  $P$ . Through examining the free energies  $G(T, P)$  of possible crystal phases, phase changes can be monitored by varying two thermodynamic parameters. In our calculations, the Gibbs free energy  $G$  is obtained from minimizing the availability or non-equilibrium Gibbs free energy ( $G^*$ ) with respect to the

volume  $V$  at a given  $T$  and  $P$  as follows.<sup>44</sup>

$$G(T, P) = \min_V [U_{el}(V) + F_{vib}(T, V) + PV], \quad (1)$$

$$F_{vib}(T, V) = \frac{1}{2} \sum_{qj} \hbar \omega_{qj}(V) + k_B T \sum_{qj} \ln \left[ 1 - \exp \left( -\frac{\hbar \omega_{qj}(V)}{k_B T} \right) \right]. \quad (2)$$

where the index  $j$  labels the phonon modes for each crystal momentum vector  $q$ .

In the phonon calculations considering lattice anharmonicity, the most important procedure is determining IFCs. To this end, it is necessary to have structures with atoms that are displaced from their force-zero positions. If the small number of atoms are displaced, we need to have relatively large structures. Sometimes, it is necessary to have several thousands of structures even for high-symmetry cubic phase. In this case, the error for the determination of IFCs is very small since the amount of displacement is constant and the direction of displacements are along each of three orthogonal axes. Therefore, one important aspect of our methodology is the use of atomic-scale calculations to evaluate forces acting on individual atoms that are displaced from their force-zero structure. These effects do play a crucial role in determining the impact of anharmonic effects. To this purpose a first strategy consists in resorting to density functional theory<sup>45</sup> (DFT) as implemented in the Vienna ab initio simulation package (VASP).<sup>46</sup> The Perdew-Burke-Ernzerhof (PBE) version of generalized gradient approximation (GGA)<sup>47</sup> is adopted for the exchange-correlation functional. The electron-ion interactions are described by the projector augmented wave (PAW) method.<sup>48</sup> The geometries are relaxed using the conjugate gradient (CG) method until the Hellman-Feynman forces on the individual atoms become less than 0.001 eV/Å. The convergence criteria of total energy in the self-consistent field (SCF) loop is  $10^{-8}$  eV with the energy cutoff of 500 eV. The tetrahedron method with Blöchl corrections is chosen for accurate integration over the Brillouin-zone.

As a second strategy of structural sampling, we resorted to a scheme fully rooted into ab-initio molecular dynamics (AIMD).<sup>49–51</sup> We initially conducted AIMD simulations, within a Born-Oppenheimer scheme<sup>52</sup>, in the canonical NVT ensemble by setting the temperature to 300 K. The thermostat of Nosé-Hoover was implemented.<sup>53</sup> This canonical simulations lasted for 4 ps, with a time step of 2 fs. From the trajectory obtained, we sampled 80 atomic configurations at constant time intervals. Subsequently, on these configuration, all the atoms inside the simulation cell were randomly displaced by 0.1 Å. The atomic forces for the configurations prepared in this manner were obtained using DFT cal-

where  $U_{el}$  is the total electronic energy,  $G^*(T, V, P) \equiv U_{el}(V) + F_{vib}(T, V) + PV$ , and  $F_{vib}$  is the vibrational free energy. The vibrational free energy can be calculated from the QHA or anharmonic approaches using the phonon density of states. Based on QHA the vibrational free energy  $F_{vib}$  is expressed as<sup>31</sup>

culations with the energy cutoff of 500 eV and  $4 \times 4 \times 4$   $k$ -grids. The methods for structure sampling employed in this study are very much consistent with each other. However, AIMD proved more efficient and it has been mostly adopted throughout this study.

When performing SCP calculations (as implemented in ALAMODE<sup>54</sup>) one has to keep in mind that considering lattice anharmonicity is analogous to the quasiparticle GW method in the electronic structure calculations. As the GW calculations consider many-body interactions starting from Kohn-Sham eigenstates, the SCP theory considers lattice anharmonicity by solving the Dyson equation that considers phonon many-body interactions. In doing so, we need to consider three main anharmonic self-energy terms, the so-called tadpole, loop, and bubble diagrams. Each of the three terms can be calculated with cubic or quartic IFCs ( $\Phi_3, \Phi_4$ ). However, finding a fully self-consistent solution of the Green function  $G(\omega)$  in the Dyson equation including those three self-energy terms is very challenging because of the bubble self-energy term that contains an  $\omega$  dependence. Therefore the strategy of Tadano *et al.* is initially to obtain a self-consistent solution without the bubble term (SC1). Then the fully dressed Green function can be solved with the Dyson equation that contains frequency dependent bubble self-energy and the solution of SC1 as an input phonon propagator. Therefore the Dyson equation that needs to be solved can be written as follows:

$$\{G_q(\omega)\}^{-1} \approx \{G_q^S(\omega)\}^{-1} - \Sigma_q^B [G^S, \Phi_3](\omega). \quad (3)$$

Tadano *et al.* end up with the following self-consistent equation to practically deal with the above equation.<sup>19</sup>

$$\Omega_{qj}^2 = (\omega_{qj}^S)^2 - 2\omega_{qj}^S \text{Re} \Sigma_{qj}^B [G^S, \Phi_3](\omega = \Omega_{qj}) \quad (4)$$

where  $\omega_{qj}^S$  is the self-consistent solution (SC1) obtained without frequency dependent bubble self-energy term. Instead of solving for fully self-consistent solutions of Eq. (4), by putting  $\omega = \Omega_{qj}$ , we can obtain the solution similar to  $G_0W_0$  calculations in the electron many-body calculations (QP-NL). Depending on the ways that the frequency in the bubble self-energy is approximated in Eq.

(4), there are two more levels of approximations.<sup>19</sup> Those are corresponding to the cases when  $\omega = 0$  and  $\omega = \omega_{qj}^S$ , which are denoted as QP[0] and QP[S], respectively.

### III. RESULTS

#### A. Quasi-harmonic approximation results

We first performed structural optimization of various polymorphs. The optimized lattice parameter ( $a_0$ ) of primitive cubic  $\text{Na}_3\text{OCl}$  is 4.538 Å. To prepare the structures with octahedral tilting, a  $2 \times 2 \times 2$  supercell is used. As we confirmed in our previous work, the monoclinic structure with  $P2_1/m$  symmetry is the most stable in terms of static energy. If we assume the process of octahedral tilting from the  $2 \times 2 \times 2$  cubic supercell, this structure can be represented as  $a^+b^-c^-$  with the Glazer notations as shown in Fig. 1. This indicates that the structure can be represented as the combinations of octahedral tilting along each axis. Here,  $a^+b^-c^-$  means in-phase rotation of octahedra along [100] direction and the out-of-phase rotation of octahedra along [010] and [001] directions as illustrated in Fig. 1. We obtained  $a = 9.0645$  Å,  $b = 9.0625$  Å,  $c = 9.0613$  Å, and  $\alpha = 90.01^\circ$ ,  $\beta = 90.00^\circ$ ,  $\gamma = 90.00^\circ$  for the monoclinic  $P2_1/m$  in a  $2 \times 2 \times 2$  supercell consisting of 40 atoms. Compared to the lattice constant of the cubic phase, there is a 0.13 - 0.16% decrease in length along each direction. The phonon dispersions of cubic  $Pm\bar{3}m$  and 14 tilted structures are generated using a finite displacement method (see Fig. S1 in Supplemental Material<sup>55</sup>),<sup>56-58</sup> as implemented in the Phonopy code<sup>31</sup>. The QHA is used to calculate thermodynamic quantities and estimate the phase transition. For all of the 15 phases,  $2 \times 2 \times 2$  supercells with a  $4 \times 4 \times 4$   $k$ -mesh are used to ensure consistency. We also confirmed that

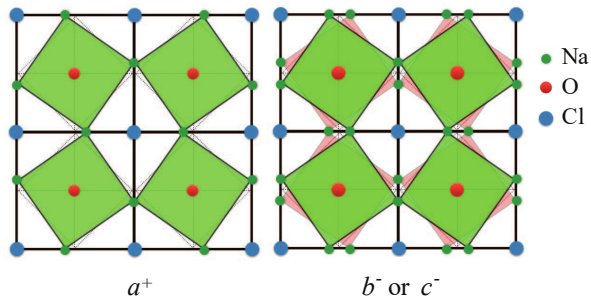


Figure 1. According to the Glazer's notation,  $P2_1/m$  structure also can be represented as  $a^+b^-c^-$ . Here,  $a^+$  means there is only in-phase rotation of  $\text{ONa}_6$  octahedra along [100] direction which is derived from atomic displacements by the  $M$  vibrational soft mode while  $b^-c^-$  means the out-of-phase rotations pattern repeats along the [010] and [001] directions induced from displacements by the  $R$  vibrational soft mode. The dotted squares are drawn to guide the  $\text{ONa}_6$  octahedra in the cubic phase and the green (front) and red (behind) squares indicate the tilted octahedra in the  $P2_1/m$  phase.

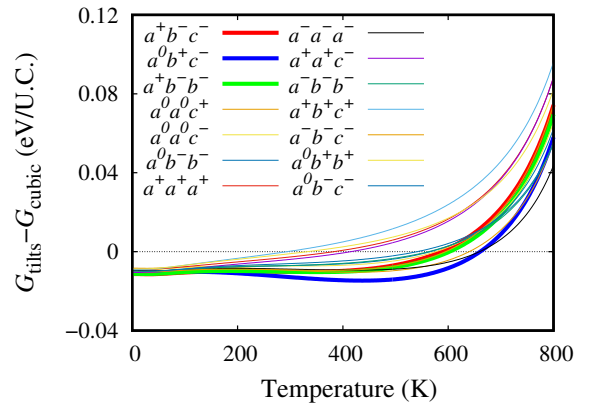


Figure 2. Temperature-dependent Gibbs free energies ( $G_{\text{tilts}}$ ) at pressure  $P = 0$  for 14 tilted structures of  $\text{Na}_3\text{OCl}$  relative to the Gibbs free energy for cubic ( $G_{\text{cubic}}$ )  $\text{Na}_3\text{OCl}$ .

the convergence of the cubic phase Gibbs free energy can be achieved with  $4 \times 4 \times 4$   $k$ -mesh as shown in Table S1 of Supplemental Material<sup>55</sup>.

The QHA results in Fig. 2 show the sequence of phase change from cubic  $Pm\bar{3}m$  to orthorhombic  $Bmmb$  (denoted by  $a^0b^+c^-$ ) and then to monoclinic  $P2_1/m$  (denoted by  $a^+b^-c^-$ ). The cubic phase is the most stable phase at high temperature and low pressure, and it has a phase transitions to the orthorhombic phase at around 650 K. The orthorhombic  $Bmmb$  phase is a tilted phase that results from the condensation of imaginary  $M$  and  $R$  soft modes. The condensation of the soft mode at  $M$  causes in-phase rotation along the  $y$ -axis and the soft mode condensation at  $R$  induces out-of-phase rotation along the  $z$ -axis. With decreasing temperature, the next phase transition is to the monoclinic  $P2_1/m$  phase that is derived from a condensed  $X$  soft mode of the  $a^0b^+c^-$  phase.<sup>59</sup> This phase transition to the  $P2_1/m$  structure is also known to be induced by the combination of  $M$  and  $R$  soft phonon condensation from the cubic phase. According to the quasi-harmonic phonon calculations, this phase transition is predicted to occur at around 135 K.

To check the convergence of harmonic force constants with respect to the supercell size, we calculated the root-mean-square (RMS) of the difference of force constants. When the RMS is calculated with the force constants of  $4 \times 4 \times 4$  supercell as the reference, we found that the RMS values of  $1 \times 1 \times 1$ ,  $2 \times 2 \times 2$ , and  $3 \times 3 \times 3$  supercells are 0.4393, 0.0242, and, 0.0056, respectively. Moreover, we also checked the convergence of free energy in different cell sizes. The results show that the free energy differences of the cubic phase between  $2 \times 2 \times 2$  supercell and  $3 \times 3 \times 3$ ,  $4 \times 4 \times 4$ , and  $6 \times 6 \times 6$  supercells are greater than  $10^{-2}$  eV per unit cell (UC). These energy differences are larger than the free energy differences between cubic and titled phases and, in turn, this results in a large error in the phase transition temperature. However, we confirmed that in the case of  $4 \times 4 \times 4$  supercell, the free energy converges within  $10^{-3}$  eV/UC. Therefore, 3 phases

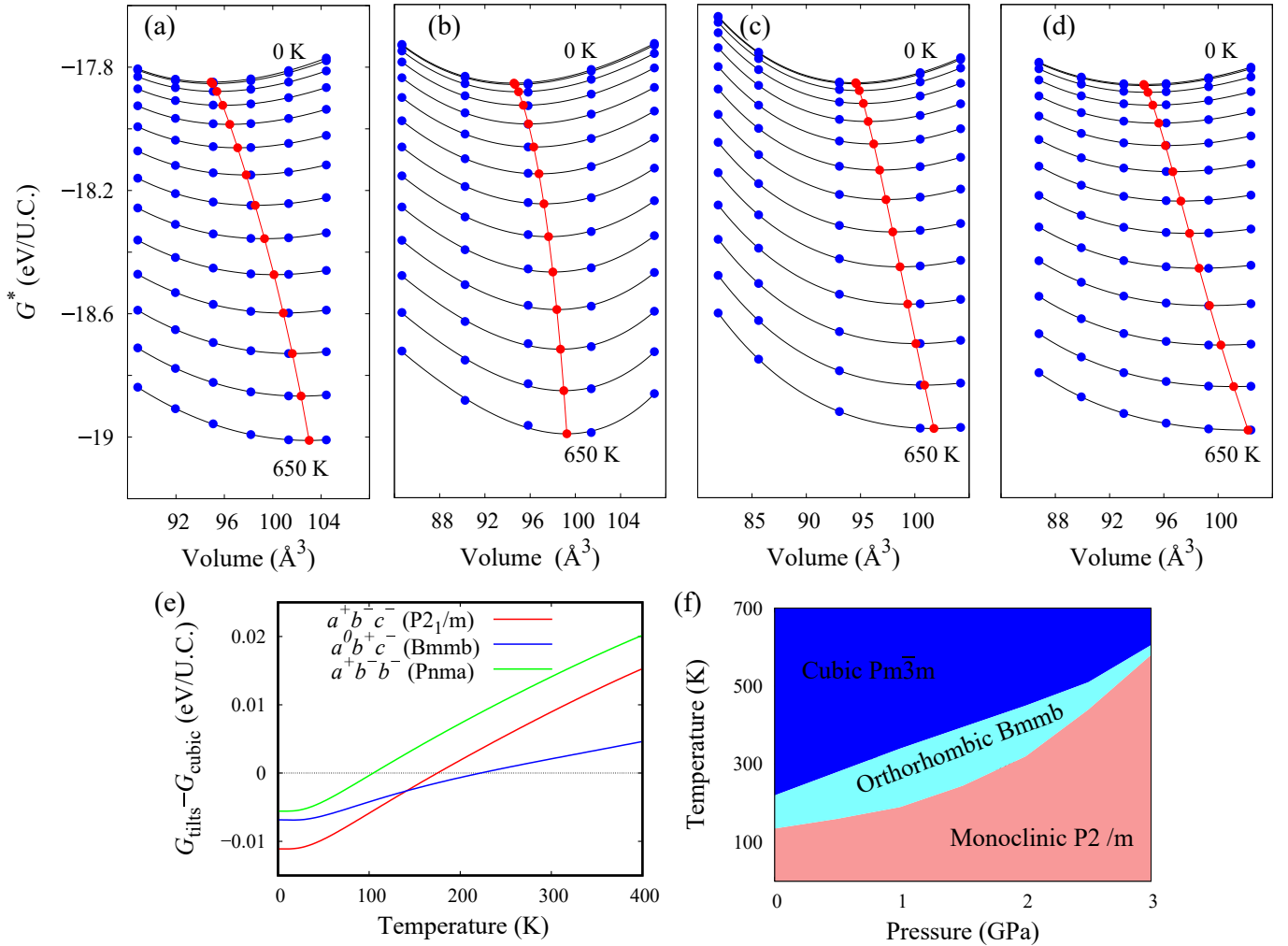


Figure 3. Non-equilibrium Gibbs free energies  $G^*(T, V, P)$  for the (a) cubic  $Pm\bar{3}m$ , (b) orthorhombic  $Bmmb$ , and (c) monoclinic  $P2_1/m$ , and (d) orthorhombic  $Pnma$  phases with respect to volume at 0 pressure and different temperatures between 0 K to 650 K are presented by blue circles with black curves fitted to the Birch-Murnaghan equation of states. From the minima of the respective black curves, the Gibbs free energies at zero pressure are obtained, and they are shown with red circles and connected with red lines. (e) The Gibbs free energy difference of the orthorhombic  $Bmmb$ , orthorhombic  $Pnma$  and monoclinic  $P2_1/m$  phases were comparable to the cubic phase. (f)  $P$ - $T$  phase diagram of  $Na_3OCl$ .

involved in the phase transition, the  $4 \times 4 \times 4$  supercell (320 atoms) with the  $2 \times 2 \times 2$   $k$ -mesh is used to ensure the consistency. Figs. 3(a-d) show the non-equilibrium Gibbs free energies of four phases of  $Na_3OCl$ . From the minimum at each temperature curve, the Gibbs free energy  $G$  is determined. The difference in the Gibbs free energies between the tilted phase and the cubic phase is shown in Fig. 3(e), and it shows that the cubic phase is stabilized at temperatures higher than 220 K. The orthorhombic  $Bmmb$  phase is stabilized in the range between 135 K and 220 K. The convergence of the cubic-to-orthorhombic phase transition temperature with respect to the supercell size is shown in Fig. S2 of Supplemental Material<sup>55</sup>.

This phase transition result is consistent with the experimental observation stating that the cubic structure is the most stable phase at room temperature and ambi-

ent pressure.<sup>11</sup> The phase diagram can be generated by calculating Gibbs free energies as a function of the temperature for the given six different pressures which are obtained by Eq. (1). Fig. 3(f) shows that the room temperature stable phase is the lower symmetry phase when the pressure is higher than 0.7 GPa. We propose that  $Na_3OCl$  is in the monoclinic  $P2_1/m$  phase at a pressure over 2.1 GPa and room-temperature conditions. The orthorhombic phase is observed in the range of pressure between 0.7 and 2.1 GPa, and cubic phase is considered to be the most stable at the pressure below 0.7 GPa.

## B. Self-consistent phonon calculations

Due to the relatively small computational cost of phonon calculations with QHA, we were able to ex-

amine 3 different polymorphs and plot the phase diagram with respect to temperature and pressure. Despite this advantage, it is also well known that QHA has a limitation in the description of lattice anharmonicity. Therefore we additionally performed self-consistent phonon (SCP) calculations using ALAMODE.<sup>54</sup> It considers not only the second but also fourth-order IFCs at the same time, which enables the description of phonon frequency change with respect to temperature.<sup>14,60</sup> We also note that previous calculations on oxide or halide perovskites already demonstrated that SCP calculations of the high-symmetry cubic phase are useful for prediction of the phase transition temperature. The literature reports that particular soft phonons lead to phase transition by phonon condensation. Given the structural similarity of Na<sub>3</sub>OCl with the perovskite materials, we need to pay attention to the possibility of observing similar behavior.<sup>14</sup>

After finishing force calculations for all sampled structures, we need to determine IFCs out of raw data. This can be understood as the fitting of IFCs using DFT force data. Therefore there could be many detailed choices, including regularization methods that are frequently used in the machine learning to prevent overfitting. However, we found that simple ordinary least square (OLS) fitting works well here. Sometimes, harmonic force constants are determined first with finite displacement sampling and then the other higher orders of IFCs are determined with predetermined harmonic FC fixed. This is the preferred way of fitting since it reduces the possible errors of harmonic FC in the case when all orders of IFCs are determined simultaneously. Here, we found that resulting phonon band structures do not change much even when all orders of IFCs are determined simultaneously. Although IFCs up to quartic terms are used in the SCP calculations, higher orders up to the sixth IFCs are also determined for the accuracy of IFCs that we are going to use.<sup>14,60</sup> All possible combinations of interactions were considered for harmonic and cubic terms, and the combinations with the distance between atoms less than 12 bohr, 8 bohr, and 8 bohr were considered for the fourth, fifth, and sixth-order IFCs, respectively.

There are imaginary frequencies in the phonon band structures of 12 octahedral tilted structures. However, those imaginary frequencies are neglected in the calculation of vibrational free energy. Moreover, the strong lattice anharmonicity found in perovskite materials raises the need of applying this method, including the consideration of lattice anharmonicity in the antiperovskite Na<sub>3</sub>OCl. For the consideration of lattice anharmonicity, we need to prepare a quartic order of interatomic force constants. However, lower symmetry structures require a formidable amount of interatomic force constants. Therefore, here we considered only the high symmetry cubic phase. The phonon band structure of the cubic Na<sub>3</sub>OCl phase shows imaginary frequencies at  $M$  and  $R$  symmetry points. If we consider lattice anharmonicity, these imaginary frequencies modes turn into soft phonon

modes with positive frequency. In addition, they tend to have strong temperature dependence and disappear below a certain temperature. Therefore, through those calculations, we will be able to predict the phase transition temperature. Moreover, the lower energy structure can be viewed as a small modification of the higher-symmetry structure. Because the modification is caused by the distortion corresponding to the eigenvector of the modes with the imaginary frequency, we can predict the symmetry of the low-temperature phase. With this in mind, we performed SCP calculations as implemented in ALAMODE<sup>54</sup>. In Fig. 4(a), the anharmonic phonon band structures of cubic Pm $\bar{3}$ m Na<sub>3</sub>OCl calculated with the SC1 method is shown in the range of temperatures from 200 K to 500 K. We can recognize that by including the fourth-order IFC in the SCP equation, the imaginary phonon frequencies disappear. In doing that, we also found that the  $q$ -mesh of  $8 \times 8 \times 8$  is a reasonable choice in terms of the convergence of soft mode frequencies at  $M$  and  $R$  symmetry points (see Table S2 in Supplemental Material<sup>55</sup>). As shown in Fig. 4(b), the soft mode frequencies at  $M$  and  $R$  can be nicely fitted with the equation,  $\Omega_q^2(T) = a(T - T_c)$ . From Fig. 4(b), the result shows that the orthorhombic-to-cubic phase transition occurs at around 86 K, which is an underestimate compared to the QHA result with the  $3 \times 3 \times 3$  supercell. It is consistent with the theory that QHA method neglects the imaginary frequencies while the anharmonic approach takes into account the effect of these phonon modes. Accordingly, the vibrational energy decreases in consequence lowering the free energy of the cubic phase.

The calculated anharmonic phonon dispersion curves using SC1 approximation are compared to the one using the QP method by including bubble self-energy in Figs. 4(c,d). The SC1 phonon frequencies are overestimated compared to the QP frequencies, and the overestimation is significant in the soft mode while the QP[0] and QP[S] results are close to the QP-NL one. The QP[0] frequencies are slightly underestimated in the optical modes while the QP[S] results are consistent with the QP-NL ones. Similar to SC1 characteristic, through linear fitting of the temperature dependence of squared phonon frequencies, we can estimate the phase transition temperature as given in Table. I. The QP theory with different treatments gives similar results of about 195 K, which is more than two times higher than the transition temperature from the SC1 method and a similar report is given by Tadano *et al.*. By including the bubble self-energy term on top of the SC1 solution they found that the phase transition temperatures of halide perovskite become close to the experimental ones.<sup>19</sup> Their estimation of the transition temperature without the bubble term was almost half of the value compared to the experimental one. However, by including the bubble term, they were able to improve the results significantly. Unfortunately, the experimental phase transition temperatures of Na<sub>3</sub>OCl have not been reported yet. Therefore, direct comparison with the experimental data is not available

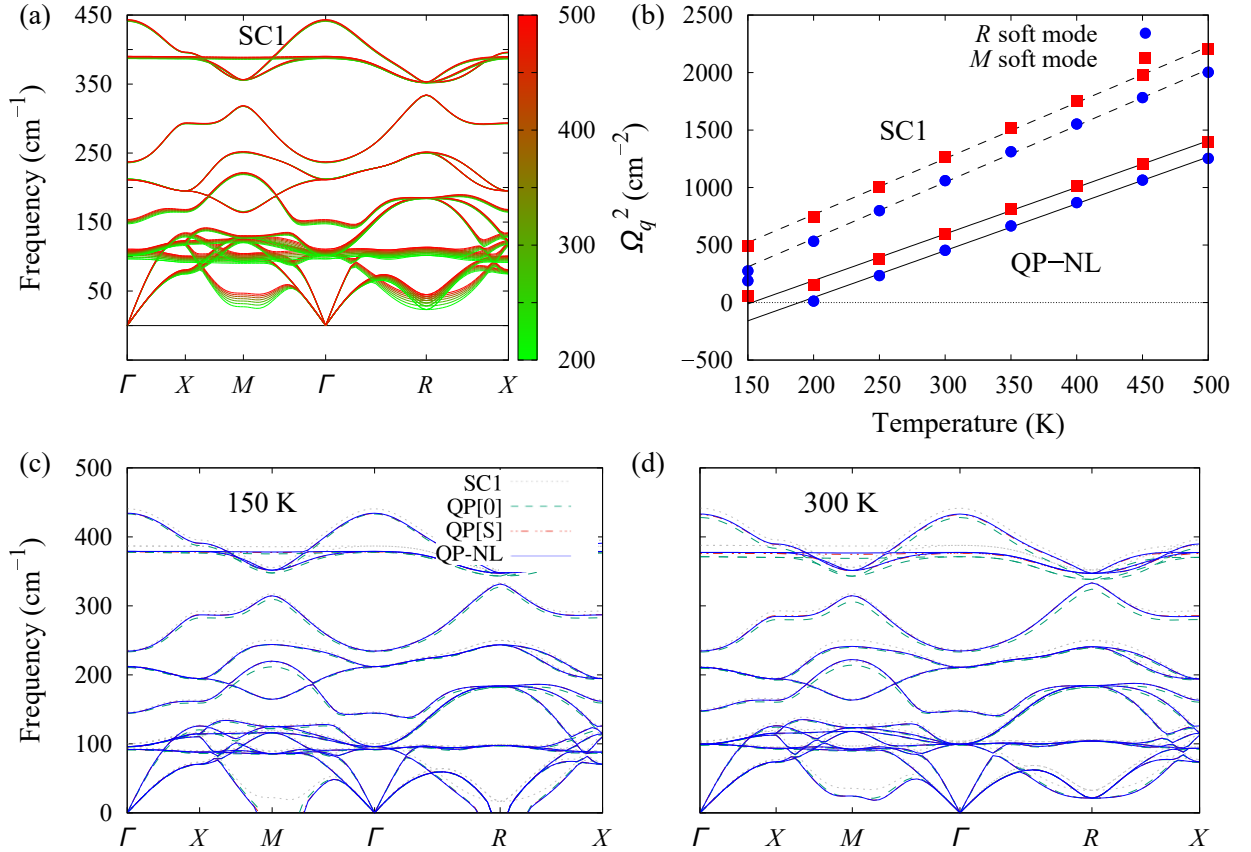


Figure 4. (a) Phonon band structure at various temperatures from 200 K to 500 K by considering the fourth-order anharmonic contribution. (b) Temperature dependence of the squared phonon frequencies at the  $M$  and  $R$  modes. (c, d) Anharmonic phonon dispersion curves of cubic  $\text{Na}_3\text{OCl}$  calculated at 150 K and 300 K (below and above  $T_C$ ) using different treatments of QP theory. The red dotted lines, green dashed lines, black dash-double-dotted lines, and blue solid lines represent the phonon bands obtained from SC1, QP[0], QP[S], and QP-NL, respectively.

at this point. Nonetheless, its room-temperature stability of the cubic phase reported in the literature suggests that the current computational predictions are at least in a reasonable range.

The materials with strong lattice anharmonicity also tend to be sensitive to external strain. Therefore we need to carefully consider the effect of thermal expansion on the phase transition temperature. For reliable prediction of thermal expansion, we adopted the PBEsol exchange-correlation functional. It is demonstrated that the lattice constant calculated with PBEsol functional<sup>61</sup> is close to the experimental one compared to that estimated with other functionals such as PBE or LDA. Please note that, without temperature effect, the lattice constant of cubic phase is 4.483 Å which is smaller than PBE lattice constant (4.538 Å) by 1.2%. To consider temperature effect on the lattice constant, thermal expansion of cubic  $\text{Na}_3\text{OCl}$  is calculated with the Helmholtz free energy curves at various temperatures as presented in Fig. 5(a). The minimum points of energy-lattice constant curves at each temperature are marked with blue squares. As shown in Fig. 5(b), the lattice constant increases almost linearly with increasing temperature. However, we need

to keep in mind that thermal expansion curve is plotted from the calculations with fixed lattice constant. Therefore, it is necessary to have different information which shows the relationship between lattice constant versus  $T_C$ . For the estimation of  $T_C$ , as shown in Fig. 5(c), a linear relation of square frequencies at  $M$  and  $R$  soft modes is used. Note that for the thermal expansion we used self-consistent phonon calculations (SC1), however for the estimation of  $T_C$ , we used phonon band structures calculated with additional self-energy term that has frequency dependence (QP-NL). The data in Fig. 5(c) are the particular case when the lattice constant is obtained at an energy minimum with the PBEsol functional. We can easily recognize that the frequencies at two soft modes are so close, which results in the phase transition temperature at similar temperatures (152 - 183 K) by the condensation of each soft mode. As shown in Fig. 5(b), when the lattice constant increases, the estimated  $T_C$  decreases. The crossing point of thermal expansion line and lattice constant versus  $T_C$  curve indicates the phase transition point after considering thermal expansion. In comparison with  $T_C$  in Fig. 5(c) which assumes a fixed lattice constant, the consideration of thermal expansion



Method	Range of transition temperatures (K)
SC1	54 - 86
QP[0]	168 - 195
QP[S]	167 - 195
QP-NL	166 - 195

Table I. Cubic-to-orthorhombic phase transition temperatures are calculated by the QP theory at different levels. Two values in each cell show the transition temperatures estimated from the soft mode frequency at  $M$  and  $R$  points, respectively

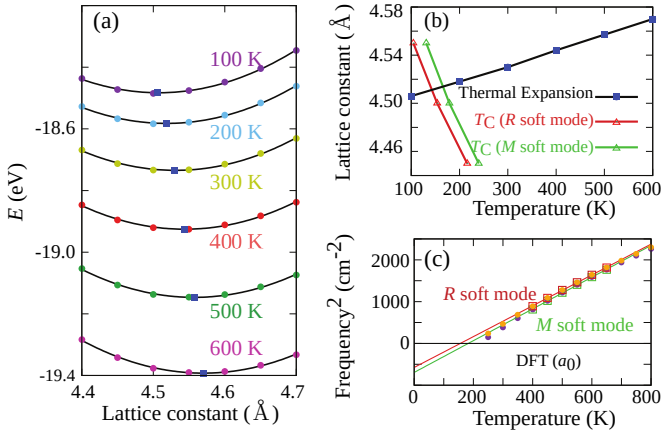


Figure 5. (a) Helmholtz free energy curves at various temperatures from 100 to 600 K. The minimum points at each temperature curves are marked with blue squares. (b) Thermal expansion curve and lattice constant versus phase transition temperature  $T_C$  curve. (c) Temperature dependence of the squared phonon frequencies at the  $M$  and  $R$  modes when the lattice constant is obtained at energy minimum with the PBEsol functional. The data points marked with empty squares are used for line fitting.

makes  $T_C$  lower by 16 - 21 K (136 vs 152 K and 162 vs 183 K). The effect of thermal expansion seems to be not so significant in this particular material. However, as shown in Fig. 5(b), this can be dependent on how the soft mode frequency changes when the lattice constant increases.

Electronic structure and ionic transport properties of

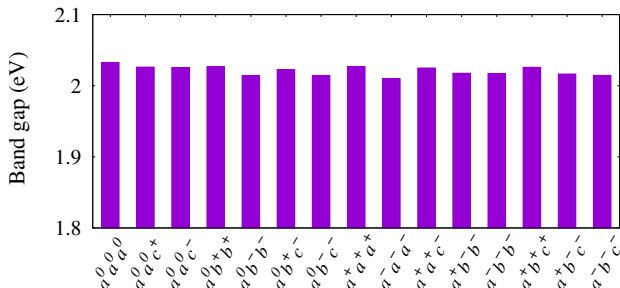


Figure 6. Band gaps for 15 phases of  $\text{Na}_3\text{OCl}$

$\text{Na}_3\text{OCl}$  are important as the safety and efficiency indicators for electrolyte applications. Since electrolyte is not supposed to conduct electricity for safety, we calculated the electronic band gaps of the 14 tilted phases including the cubic phase and found that the band gaps of all the phases fall in the range between 2.01 eV and 2.03 eV when we used the GGA functional as shown in Fig. 6. In the previous report by Pham *et al.*<sup>17</sup>, the band gaps of cubic and monoclinic phases increased to around 3.40 eV when the hybrid functional Hied-Scuseria-Erznerhof (HSE) method is used while the band gaps are around 2 eV when the GGA functional is used<sup>62</sup>. From these results, we may consider  $\text{Na}_3\text{OCl}$  as an insulator in all the tilted phases. Secondly, the ionic transport property is obtained by calculating the migration energy barriers of Na via the vacancy-mediated mechanism<sup>2</sup> with the nudged elastic band (NEB) method<sup>63</sup> for cubic  $\text{Pm}\bar{3}\text{m}$ , orthorhombic  $\text{Bmmb}$ , and monoclinic  $\text{P}2_1/\text{m}$  phases. NEB calculation is performed in a supercell of 40 atoms. The energy convergence criterion is set to  $10^{-3}$  eV and five intermediate NEB images are used. Fig. 7(a-c) show the possible reaction paths of vacancy migration in a schematic way; the  $\text{Pm}\bar{3}\text{m}$  phase has only one path, but the  $\text{Bmmb}$  and  $\text{P}2_1/\text{m}$  phases have 6 and 12 paths, respectively. Figs. 7(d-f) show the calculated minimum energy paths for sodium vacancy migration from one Na site to another in cubic  $\text{Pm}\bar{3}\text{m}$ , orthorhombic  $\text{Bmmb}$ , and monoclinic  $\text{P}2_1/\text{m}$  phases. There are six available migration paths in orthorhombic  $\text{Bmmb}$  made of three symmetrically distinct Na sites,<sup>64</sup> and twelve paths in  $\text{P}2_1/\text{m}$  composed of four symmetrically distinct Na sites (see Table S3 and S4 in Supplemental Material for Wyckoff positions in orthorhombic  $\text{Bmmb}$  and monoclinic  $\text{P}2_1/\text{m}$ <sup>55</sup>). The single vacancy migration energies are 0.32 - 0.35 eV (average 0.34 eV) for monoclinic  $\text{P}2_1/\text{m}$ , 0.31 - 0.35 eV (average 0.34 eV) for orthorhombic  $\text{Bmmb}$ , and 0.30 eV for cubic, respectively. The distorted structures ( $\text{P}2_1/\text{m}$  and  $\text{Bmmb}$  phases) are shown to have not much variation in migration energy barriers compared to the cubic one. For cubic phase, the energy barrier (0.30 eV) that we obtained falls between the range of previous reports; the activation energy is 0.29 eV by Ahiavi *et al.*<sup>65</sup> and the migration energy barrier is 0.43 eV by Wang *et al.*<sup>66</sup>

### C. Conclusions

In summary, two types of phonon calculations are performed to investigate the phase transition of antiperovskite  $\text{Na}_3\text{OCl}$ . The first one is quasi-harmonic phonon calculations. When the Gibbs free energies of 14 different polymorphs are calculated with the QHA, the  $P$ - $T$  phase diagram shows that three stable phases would appear in the limited scopes of temperature and pressure. At ambient pressure, the high-symmetry cubic phase with  $\text{Pm}\bar{3}\text{m}$  symmetry is expected to be stable at the temperature above 205 K and monoclinic phase with  $\text{P}2_1/\text{m}$  symmetry becomes stable below 135 K. In the temperature

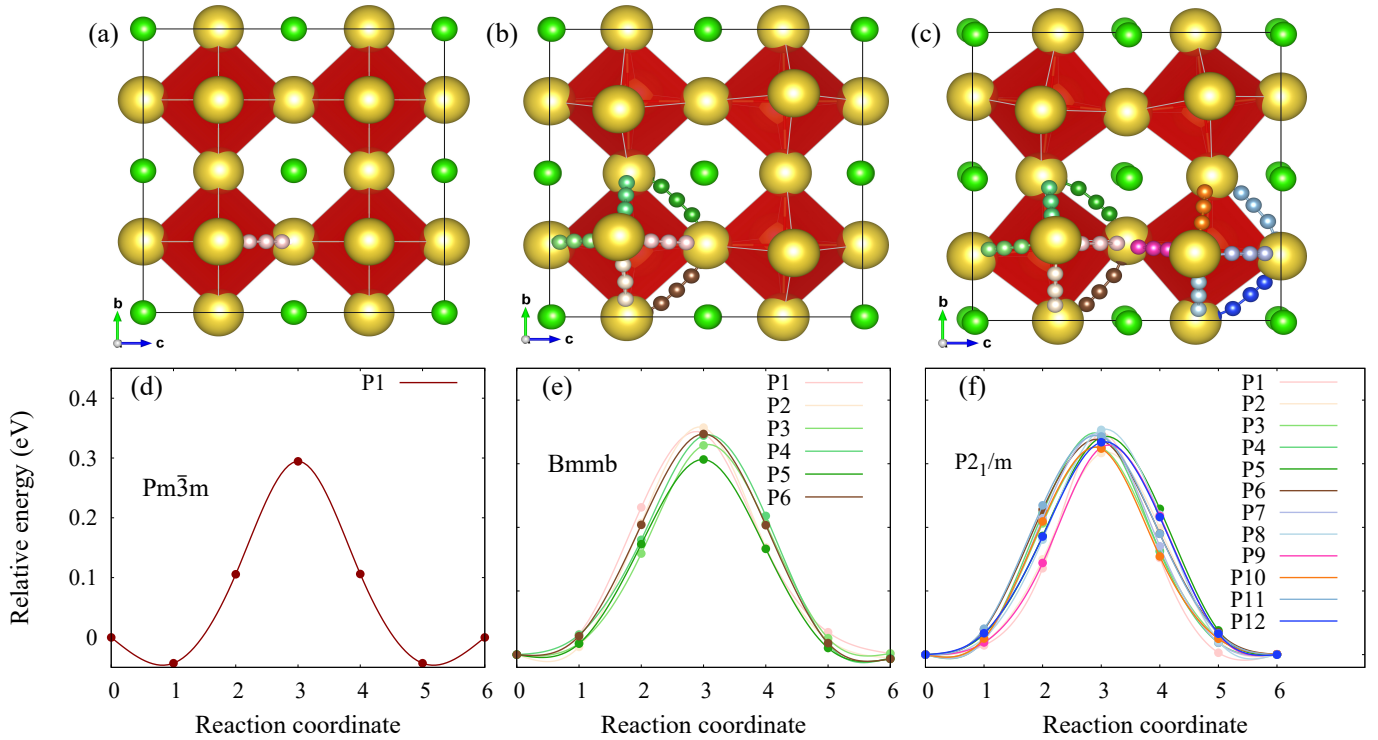


Figure 7. Reaction paths for Na migration are shown with the small colored spheres in (a) cubic  $Pm\bar{3}m$ , (b) orthorhombic  $Bmmb$ , and (c) monoclinic  $P2_1/m$  phases and Na, O, and Cl atoms with the larger yellow, red (inside the red octahedra), and green spheres, respectively. The relative energy changes of vacancy migration through the minimum energy path in (d) cubic  $Pm\bar{3}m$ , (e) orthorhombic  $Bmmb$ , and (f) monoclinic  $P2_1/m$  phases are illustrated with colors for the corresponding reaction paths.

range between 135 K and 205 K,  $Bmmb$  is expected to be most stable structure. The second one is the inclusion of anharmonic terms in the phonon calculations by using quartic and cubic IFCs. The phase transition temperatures ( $T_C$ ) are calculated with the basic self-consistent phonon calculations (SC1) as well as the temperature-dependent phonon band structures calculated with additional consideration of the bubble self-energy term (QP-NL). Since the latter method corrects the overestimation of soft mode frequency, more than twice of phase transition temperature is expected using the former one (54 - 86 K vs 166 - 195 K). The effect of thermal expansion on  $T_C$  is not significant in cubic  $Na_3OCl$ . Nonetheless, our method shows that the behavior of the soft mode upon lattice constant change could play a critical role in the theoretical determination of thermal expansion effects on  $T_C$ . The overall results are consistent with the previous computational report on halide perovskite  $\alpha$ - $CsPbBr_3$  and experimentally confirmed room temperature stability of cubic  $Na_3OCl$ . For the three vibrationally stable phases, we calculated migration energy barriers of Na vacancy, and found that the energy barriers falling in the range from 0.30 to 0.34 eV are not much different in phases.

## ACKNOWLEDGMENTS

This work was supported by the National Research Foundation of Korea (NRF) grants funded by the Korea government (MSIT) (No. 2021R1F1A1048555). The authors wish to thank Dr. Terumasa Tadano, researcher at National Institute for Material Science (NIMS, Japan), for his helpful comments and discussions.

## REFERENCES

- <sup>1</sup>Y. Zhao and L. L. Daemen, Superionic Conductivity in Lithium-Rich Anti-Perovskites, *J. Am. Chem. Soc.* **134**, 15042 (2012).
- <sup>2</sup>A. Emly, E. Kioupakis, and A. Van der Ven, Phase Stability and Transport Mechanisms in Antiperovskite  $Li_3OCl$  and  $Li_3OBr$  Superionic Conductors, *Chem. Mater.* **25**, 4663 (2013).
- <sup>3</sup>K. Chayambuka, G. Mulder, D. L. Danilov, and P. H. L. Notten, From Li-Ion Batteries toward Na-Ion Chemistries: Challenges and Opportunities, *Adv. Energy Mater.* **10**, 2001310 (2020).
- <sup>4</sup>H. Nguyen, S. Hy, E. Wu, Z. Deng, M. Samiee, T. Yersak, J. Luo, S. P. Ong, and Y. S. Meng, Experimental and Computational Evaluation of a Sodium-Rich Anti-Perovskite for Solid State Electrolytes, *J. Electrochem. Soc.* **163**, A2165 (2016).
- <sup>5</sup>J.-Y. Hwang, S.-T. Myung, and Y.-K. Sun, Sodium-ion batteries: present and future, *Chem. Soc. Rev.* **46**, 3529 (2017).
- <sup>6</sup>K. Li, J. Zhang, D. Lin, D.-W. Wang, B. Li, W. Lv, S. Sun, Y.-B. He, F. Kang, Q.-H. Yang, L. Zhou, and T.-Y. Zhang, Evolution of the electrochemical interface in sodium ion batteries with ether electrolytes, *Nat. Commun.* **10**, 725 (2019).

- <sup>7</sup>M. H. Braga, N. S. Grundish, A. J. Murchison, and J. B. Goodenough, Alternative strategy for a safe rechargeable battery, *Energy Environ. Sci* **10**, 331 (2017).
- <sup>8</sup>M. Wu, B. Xu, X. Lei, K. Huang, and C. Ouyang, Bulk properties and transport mechanisms of a solid state antiperovskite Li-ion conductor  $\text{Li}_3\text{OCl}$ : insights from first principles calculations, *J. Mater. Chem. A* **6**, 1150 (2018).
- <sup>9</sup>I. Hanghofer, G. J. Redhammer, S. Rohde, I. Hanzu, A. Senyshyn, H. M. R. Wilkening, and D. Rettenwander, Untangling the Structure and Dynamics of Lithium-Rich Antiperovskites Envisaged as Solid Electrolytes for Batteries, *Chem. Mater.* **30**, 8134 (2018).
- <sup>10</sup>R. Chen, W. Qu, X. Guo, L. Li, and F. Wu, The pursuit of solid-state electrolytes for lithium batteries: from comprehensive insight to emerging horizons, *Mater. Hor.* **3**, 487 (2016).
- <sup>11</sup>K. Hippler, S. Sitta, P. Vogt, and H. Sabrowsky, Structure of  $\text{Na}_3\text{OCl}$ , *Acta Crystallogr. C. Struct. Commun.* **46**, 736 (1990).
- <sup>12</sup>M.-H. Chen, A. Emly, and A. Van der Ven, Anharmonicity and phase stability of antiperovskite  $\text{Li}_3\text{OCl}$ , *Phys. Rev. B* **91**, 214306 (2015).
- <sup>13</sup>M. H. Braga, J. A. Ferreira, V. Stockhausen, J. E. Oliveira, and A. El-Azab, Novel  $\text{Li}_3\text{ClO}$  based glasses with superionic properties for lithium batteries, *J. Mater. Chem A* **2**, 5470 (2014).
- <sup>14</sup>T. Tadano and S. Tsuneyuki, Self-consistent phonon calculations of lattice dynamical properties in cubic  $\text{SrTiO}_3$  with first-principles anharmonic force constants, *Phys. Rev. B* **92**, 054301 (2015).
- <sup>15</sup>M. C. Oliveira, R. A. P. Ribeiro, E. Longo, M. R. D. Bomio, F. V. Motta, and S. R. de Lazaro, Temperature dependence on phase evolution in the  $\text{BaTiO}_3$  polytypes studied using ab initio calculations, *Int. J. Quantum Chem.* **120**, e26054 (2020).
- <sup>16</sup>M.-J. Zhou, Y. Wang, Y. Ji, Z.-K. Liu, L.-Q. Chen, and C.-W. Nan, First-principles lattice dynamics and thermodynamic properties of pre-perovskite  $\text{PbTiO}_3$ , *Acta Mater.* **171**, 146 (2019).
- <sup>17</sup>T.-L. Pham, A. Samad, H. J. Kim, and Y.-H. Shin, Computational predictions of stable phase for antiperovskite  $\text{Na}_3\text{OCl}$  via tilting of  $\text{Na}_6\text{O}$  octahedra, *J. Appl. Phys.* **124**, 164106 (2018).
- <sup>18</sup>S. A. Khandy, I. Islam, A. Laref, M. Gogolin, A. K. Hafiz, and A. M. Siddiqui, Electronic structure, thermomechanical and phonon properties of inverse perovskite oxide ( $\text{Na}_3\text{OCl}$ ): An ab initio study, *Int. J. Energy Res.* **44**, 2594 (2020).
- <sup>19</sup>T. Tadano and W. A. Saidi, First-principles phonon quasiparticle theory applied to a strongly anharmonic halide perovskite, *Phys. Rev. Lett.* **129**, 185901 (2022).
- <sup>20</sup>T. Tadano and S. Tsuneyuki, Quartic Anharmonicity of Rattlers and Its Effect on Lattice Thermal Conductivity of Clathrates from First Principles, *Phys. Rev. Lett.* **120**, 105901 (2018).
- <sup>21</sup>T. F. J. Dawson and K. Johnston, Anti-perovskites for solid-state batteries: recent developments, current challenges and future prospects, *J. Mater. Chem.* **9**, 18746 (2021).
- <sup>22</sup>J. Xie, S. de Gironcoli, S. Baroni, and M. Scheffler, First-principles calculation of the thermal properties of silver, *Phys. Rev. B* **59**, 965 (1999).
- <sup>23</sup>N. Mounet and N. Marzari, First-principles determination of the structural, vibrational and thermodynamic properties of diamond, graphite, and derivatives, *Phys. Rev. B* **71**, 205214 (2005).
- <sup>24</sup>W. Yu, C. Jin, and A. Kohlmeier, First principles calculation of phonon dispersion, thermodynamic properties and B1-to-B2 phase transition of lighter alkali hydrides, *J. Phys. Condens. Matter* **19**, 086209 (2007).
- <sup>25</sup>Z.-G. Mei, S.-L. Shang, Y. Wang, and Z.-K. Liu, Density-functional study of the thermodynamic properties and the pressure-temperature phase diagram of Ti, *Phys. Rev. B* **80**, 104116 (2009).
- <sup>26</sup>P. A. Korzhavyi and J. Zhang, Free Energy of Metals from Quasi-Harmonic Models of Thermal Disorder, *Metals* **11**, 195 (2021).
- <sup>27</sup>W. I. Choi, D. J. Yang, D. W. Jung, W.-J. Son, M. Shim, I. Jang, and D. S. Kim, Ab-initio prediction of temperature-dependent dielectric constants and curie temperatures of cubic phase perovskite materials, *MRS Commun.* **11**, 436 (2021).
- <sup>28</sup>W. I. Choi, J. S. An, I. Jang, and D. S. Kim, Strain and temperature-dependent dielectric permittivity of cubic  $\text{SrTiO}_3$ : Self-consistent phonon theory calculations, *Curr. Appl. Phys.* **29**, 78 (2021).
- <sup>29</sup>Y. Zhao, C. Lian, S. Zeng, Z. Dai, S. Meng, and J. Ni, Anomalous electronic and thermoelectric transport properties in cubic  $\text{Rb}_3\text{AuO}$  antiperovskite, *Phys. Rev. B* **102**, 094314 (2020).
- <sup>30</sup>Y. Zhao, C. Lian, S. Zeng, Z. Dai, S. Meng, and J. Ni, Quartic anharmonicity and anomalous thermal conductivity in cubic antiperovskites  $\text{A}_3\text{BO}$  ( $\text{A} = \text{K}, \text{Rb}; \text{B} = \text{Br}, \text{Au}$ ), *Phys. Rev. B* **101**, 184303 (2020).
- <sup>31</sup>A. Togo and I. Tanaka, First principles phonon calculations in materials science, *Scr. Mater.* **108**, 1 (2015).
- <sup>32</sup>D. C. Wallace, *Thermodynamics of Crystals* (Dover Publications, Mineola, New York, 1998).
- <sup>33</sup>A. Otero-de-la-Roza, D. Abbasi-Piézrez, and V. Luaña, GIBBS2: A new version of the quasiharmonic model code. II. Models for solid-state thermodynamics, features and implementation, *Comput. Phys. Commun.* **182**, 2232 (2011).
- <sup>34</sup>A. Togo, L. Chaput, I. Tanaka, and G. Hug, First-principles phonon calculations of thermal expansion in  $\text{Ti}_3\text{SiC}_2$ ,  $\text{Ti}_3\text{AlC}_2$ , and  $\text{Ti}_3\text{GeC}_2$ , *Phys. Rev. B* **81**, 174301 (2010).
- <sup>35</sup>M. Blanco, E. Francisco, and V. Luaña, GIBBS: isothermal-isobaric thermodynamics of solids from energy curves using a quasi-harmonic Debye model, *Comput. Phys. Commun.* **158**, 57 (2004).
- <sup>36</sup>Y. Oba, T. Tadano, R. Akashi, and S. Tsuneyuki, First-principles study of phonon anharmonicity and negative thermal expansion in  $\text{ScF}_3$ , *Phys. Rev. Mater.* **3**, 033601 (2019).
- <sup>37</sup>T. D. Huan, V. Sharma, G. A. Rossetti, and R. Ramprasad, Pathways Towards Ferroelectricity in Hafnia, *Phys. Rev. B* **90**, 064111 (2014).
- <sup>38</sup>B.-T. Wang, P. Zhang, R. Lizárraga, I. Di Marco, and O. Eriksson, Phonon spectrum, thermodynamic properties, and pressure-temperature phase diagram of uranium dioxide, *Phys. Rev. B* **88**, 104107 (2013).
- <sup>39</sup>Z. Deng, Z. Wang, I.-H. Chu, J. Luo, and S. P. Ong, Elastic Properties of Alkali Superionic Conductor Electrolytes from First Principles Calculations, *J. Electrochem. Soc.* **163**, A67 (2016).
- <sup>40</sup>S. G. Jabarov, D. P. Kozlenko, S. E. Kichanov, A. V. Belushkin, A. I. Mammadov, B. N. Savenko, R. Z. Mekhtieva, and C. Lathe, Structural studies of the P-T phase diagram of sodium niobate, *J. Surf. Invest. X-ray* **6**, 546 (2012).
- <sup>41</sup>M. Ahtee, A. M. Glazer, and H. D. Megaw, The structures of sodium niobate between 480 °C and 575 °C, and their relevance to soft-phonon modes, *Philos. Mag.* **26**, 995 (1972).
- <sup>42</sup>A. M. Glazer and H. D. Megaw, The structure of sodium niobate ( $\text{T}_2$ ) at 600 °C, and the cubic-tetragonal transition in relation to soft-phonon modes, *Philos. Mag.* **25**, 1119 (1972).
- <sup>43</sup>R. Lizárraga, F. Pan, L. Bergqvist, E. Holmström, Z. GerCSI, and L. Vitos, First Principles Theory of the hcp-fcc Phase Transition in Cobalt, *Sci. Rep.* **7**, 3778 (2017).
- <sup>44</sup>A. A. Maradudin, G. H. Weiss, and E. W. Montroll, *Theory of lattice dynamics in the harmonic approximation* (Academic Press, New York, 1963).
- <sup>45</sup>W. Kohn and L. J. Sham, Self-consistent equations including exchange and correlation effects, *Phys. Rev.* **140**, A1133 (1965).
- <sup>46</sup>G. Kresse and J. Furthmüller, Efficiency of ab-initio total energy calculations for metals and semiconductors using a plane-wave basis set, *Comput. Mater. Sci.* **6**, 15 (1996).
- <sup>47</sup>J. P. Perdew, K. Burke, and M. Ernzerhof, Generalized Gradient Approximation Made Simple, *Phys. Rev. Lett.* **77**, 3865 (1996).
- <sup>48</sup>G. Kresse and D. Joubert, From Ultrasoft Pseudopotentials to the Projector Augmented-Wave Method, *Phys. Rev. B* **59**, 1758 (1999).
- <sup>49</sup>R. Car and M. Parrinello, Unified approach for molecular dynamics and density-functional theory, *Phys. Rev. Lett.* **55**, 2471 (1985).
- <sup>50</sup>C. Massobrio, A. Bouzid, M. Boero, G. Ori, É. Martin, and S. L. Roux, Chalcogenide glasses for innovation in applied science: fun-

- damental issues and new insights, *J. Phys. D Appl. Phys.* **53**, 033002 (2019).
- <sup>51</sup>G. Ori, A. Bouzid, É. Martin, C. Massobrio, S. Le Roux, and M. Boero, Chalcogenide glasses as a playground for the application of first-principles molecular dynamics to disordered materials, *Solid State Sci.* **95**, 105925 (2019).
- <sup>52</sup>M. Born and O. R., Zur quantentheorie der molekeln, *Annalen der Physik* **IV. Folge**, 457 (1927).
- <sup>53</sup>W. G. Hoover, Canonical dynamics: Equilibrium phase-space distributions, *Phys. Rev. A* **31**, 1695 (1985).
- <sup>54</sup>N. R. Werthamer, Self-consistent phonon formulation of anharmonic lattice dynamics, *Phys. Rev. B* **1**, 572 (1970).
- <sup>55</sup>See Supplemental Material at.
- <sup>56</sup>D. Alfé, PHON: A program to calculate phonons using the small displacement method, *Comput. Phys. Commun.* **180**, 2622 (2009).
- <sup>57</sup>L. Chaput, A. Togo, I. Tanaka, and G. Hug, Phonon-phonon interactions in transition metals, *Phys. Rev. B* **84**, 094302 (2011).
- <sup>58</sup>K. Esfarjani and H. T. Stokes, Method to extract anharmonic force constants from first principles calculations, *Phys. Rev. B* **77**, 144112 (2008).
- <sup>59</sup>R. B. Sadok, D. Hammouténe, and N. Plugaru, New Phase Transitions Driven by Soft Phonon Modes for CsPbBr<sub>3</sub>: Density Functional Theory Study, *Phys. Status Solidi (B)* **258**, 2000289 (2021).
- <sup>60</sup>T. Tadano, Y. Gohda, and S. Tsuneyuki, Anharmonic force constants extracted from first-principles molecular dynamics: applications to heat transfer simulations, *J. Phys. Condens. Matter* **26**, 225402 (2014).
- <sup>61</sup>J. P. Perdew, A. Ruzsinszky, G. I. Csonka, O. A. Vydrov, G. E. Scuseria, L. A. Constantin, X. Zhou, and K. Burke, Restoring the density-gradient expansion for exchange in solids and surfaces, *Phys. Rev. Lett.* **100**, 136406 (2008).
- <sup>62</sup>J. Heyd and G. E. Scuseria, Efficient hybrid density functional calculations in solids: Assessment of the Heyd-Scuseria-Ernzerhof screened Coulomb hybrid functional, *J. Chem. Phys.* **121**, 1187 (2004).
- <sup>63</sup>D. Sheppard, R. Terrell, and G. Henkelman, Optimization methods for finding minimum energy paths, *J. Chem. Phys.* **128**, 134106 (2008).
- <sup>64</sup>S. Fujii, S. Gao, C. Tassel, T. Zhu, T. Broux, K. Okada, Y. Miyahara, A. Kuwabara, and H. Kageyama, Alkali-Rich Antiperovskite M<sub>3</sub>FCh (M = Li, Na; Ch = S, Se, Te): The Role of Anions in Phase Stability and Ionic Transport, *J. Am. Chem. Soc.* **143**, 10668 (2021).
- <sup>65</sup>E. Ahiavi, J. Dawson, U. Kudu, M. Courty, M. S. Islam, O. Clemens, C. Masquelier, and T. Famprikis, Mechanochemical synthesis and ion transport properties of Na<sub>3</sub>OX (X = Cl, Br, I and BH<sub>4</sub>) antiperovskite solid electrolytes, *J. Power Sources* **471**, 228489 (2020).
- <sup>66</sup>Y. Wang, Q. Wang, Z. Liu, Z. Zhou, S. Li, J. Zhu, R. Zou, Y. Wang, J. Lin, and Y. Zhao, Structural manipulation approaches towards enhanced sodium ionic conductivity in Na-rich antiperovskites, *J. Power Sources* **293**, 735 (2015).